

Precise computation of universal corner entanglement entropy at 2+1 dimension: From Ising to Gaussian quantum critical points

Ben Lee-Yeung Ngai,^{1,*} Justin Tim-Lok Chau,^{1,*} Junchen Rong,² Yuan Da Liao,^{1,†} and Zi Yang Meng^{1,‡}

¹*Department of Physics and HK Institute of Quantum Science & Technology,
The University of Hong Kong, Pokfulam Road, Hong Kong SAR, China*

²*CPHT, CNRS, Ecole Polytechnique, Institut Polytechnique de Paris, Palaiseau, France*
(Dated: December 2, 2025)

Computing the subleading logarithmic term in the entanglement entropy (EE) of (2+1)d quantum many-body systems remains a significant challenge, despite its critical role in revealing universal information about quantum states and quantum critical points (QCPs). Capitalizing on recent algorithmic advances that enable the stable calculation of EE as an exponential observable [1–3], we develop a *bubble basis* projector quantum Monte Carlo (QMC) algorithm to precisely and efficiently compute the universal corner EE along a parameter trajectory connecting the Ising and Gaussian QCPs; where in the latter case there exists an analytic value to benchmark with [4, 5]. Our approach eliminates the dominant area-law term directly within the QMC sampling, thereby promoting the coveted subleading logarithmic term to the leading contribution. We apply this technique to calculate the EE in a (2+1)d square-lattice transverse-field Ising model augmented with a four-body interaction, tracing a path from the Ising to the Gaussian QCPs and then to the first-order transition. The consistent values obtained for the universal corner EE along the path validate the reliability and precision of our approach for extracting challenging entanglement properties. These results establish the long-sought connection between the universal values of an exactly solvable limit and those of a strongly correlated regime at (2+1)d.

I. INTRODUCTION

Entanglement is the quintessential property of quantum mechanics [6–8]. As the investigation of quantum many-body states of matter advances, precise computation and quantification of the quantum entanglement therein becomes an urgent task [9, 10]. Among the many available entanglement measures, the entanglement entropy (EE) plays a central role, having already deepened our understanding and refined the classification of quantum states of matter [11–18]. For example, in (1+1)d systems, the sublinear scaling of EE with subsystem size underpins the efficiency of matrix product state representations [19]. In (2+1)d, universal contribution to EE was first identified in exactly solvable models [20, 21], and later measured in prototypical interacting models using quantum Monte Carlo (QMC) methods [12, 22]. It enabled direct probes of long-range entanglement, the structure of topological order, and the nature of the emergent fractionalized degrees of freedom.

However, a fully generic EE computation scheme for (2+1)d quantum many-body systems remains a major challenge, primarily due to the exponential complexity in accessing the wave function. An important feature of EE in (2+1)d quantum critical states is the universal corner term, i.e. the subleading logarithmic contribution to the EE. To date, analytical results for this universal term have been obtained only in free theories at (2+1)d [4, 5], for both Rényi and von Neumann entropies. For interacting theories, analytically controlled calculations have only been performed for $O(N)$ critical point in the large N approximation for the von Neumann entropy [23].

Over the years, numerous efforts have been made in developing QMC algorithm for high-precision computation of EE to extract the universal corner term at the (2+1)d Ising and $O(N)$ critical points [3, 15, 24–27]. Despite the progress, the current state of the art is still not fully satisfactory, for the following reasons

- These universal terms are subleading to the dominant area-law contribution that scales extensively with the subsystem size. Isolating the subleading contribution directly from the finite-size EE data often suffers from substantial error bars, limiting their numerical precision.
- There has been no attempt to perform benchmark study against the exactly solvable results for free theories and then compute EE across the interacting (2+1)d critical points within one set of QMC simulation. Such a setup would allow one to first quantitatively validate the QMC algorithm on reproducing the free-theory results, and only then place further confidence in the extraction of universal corner terms for the interacting quantum critical points, including a quantitative assessment of their distance from the Gaussian (free-theory) results.

It is due to these issues that the overall status of the precise computation of the universal corner coefficient for interacting QCPs remains somewhat ambiguous.

To address these challenges, we introduce in this work an advanced projector QMC (PQMC) framework based on a *bubble basis*. This development significantly improves the efficiency of the incremental SWAP algorithm for EE computation—a method recently advanced by our group [1, 3]—compared to conventional PQMC approach that employs a standard σ^z basis [24]. Furthermore, we successfully integrate the subtracted corner entanglement entropy technique [3] into this new framework. The combination of these

* These authors contributed equally

† ydliao@hku.hk

‡ zymeng@hku.hk

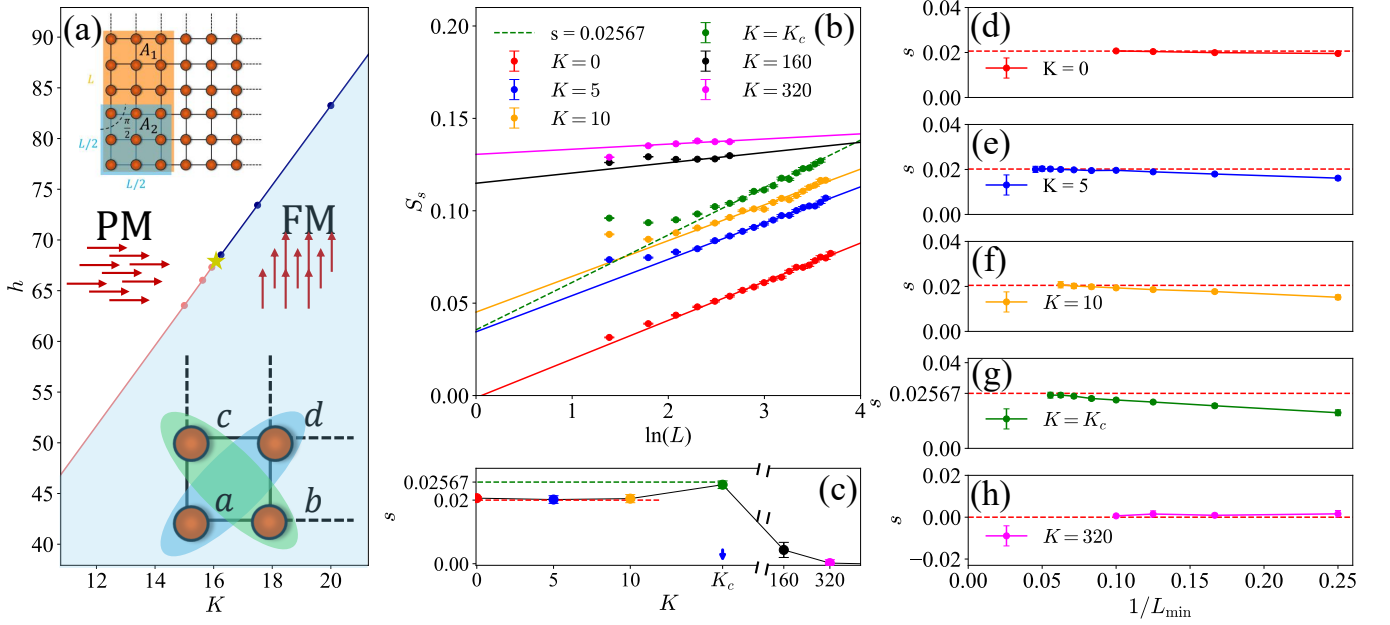


FIG. 1. Model, phase diagram and the universal corner EE from Ising to Gaussian QCPs. (a) Phase transition on $h - K$ plane. The light pink line represents the continuous phase transition, while the blue line indicates the first-order phase transition. The dots indicate the points where we performed the crossing-point analysis to determine the locations of the phase transitions. The PQC determined Gaussian fixed point is identified as the yellow star. The top left inset in (a) illustrates the entanglement regions. In a $L \times L$ square lattice, the entangled region A_1 has the dimension $L \times L/2$ (orange background) and it has a smooth boundary [Eq. (3)]. The region A_2 has a $L/2 \times L/2$ (blue background) and it has four 90° corners contribution [Eq. (4)]. The lattice is periodic along both directions (denoted by the dotted lines), and the entanglement regions A_1 and A_2 have the same boundary length. The bottom right inset in (a) illustrates the action of K -term in the Hamiltonian of Eq. (1). (b) Scaling of the subtracted entanglement entropy S_s . The dependence of S_s on $\ln(L)$ at the phase transition boundary for selected values of $K = 0, 5, 10, K_c, 160$ and 320 are shown, where $K_c = 16.02(6)$ is the Gaussian QCP. (c) The universal log-coefficient s , extracted from the data in (b), as a function of K . (d), (e), and (f) show the extrapolation for $K = 0, K = 5$, and $K = 10$ at their corresponding $(2+1)d$ Ising QCPs. The computed corner log-coefficients converge to a universal average value of $s = 0.020(1)$ as L_{\min} increases. (g) corresponds to the Gaussian fixed point at K_c , where the corner log-coefficient converges to the universal value of $s = 0.025(1)$. (h) is for $K = 320$ at its first-order phase transition point; here, the computed corner log-coefficients vanishes as $s = 0.000(1)$.

methods allows the dominant area-law term in the EE to be directly eliminated during the QMC sampling process. As a result, the coveted subleading logarithmic term becomes the leading contribution in the simulation output, enabling a precise and direct extraction of the universal corner coefficient.

We design a $(2+1)d$ square lattice transverse-field Ising model (TFIM) augmented with a four-body interaction term. By tuning the relative strength between the two-spin and four-spin couplings, a continuous parameter path can be realized, connecting the Ising and Gaussian (free-theory) QCPs and ending in a first-order transition. Applying our bubble basis incremental SWAP algorithm along this path, we extract the universal corner contribution to the EE. At the Gaussian fixed point, the resulting logarithmic coefficient for four 90° corners agrees perfectly with the analytical value of $s = 0.02567$ [4] – our QMC estimate is $s = 0.025(1)$ – the number in parentheses indicates the uncertainty in the last significant digit. This value is clearly distinguishable from the Ising universal coefficient obtained along the same path, $s = 0.020(1)$ for four 90° corners. The accurate determination of these universal terms across the $(2+1)d$ QCPs – from the Ising to the Gaussian universality class – demonstrates the reliability of our approach

in capturing challenging entanglement properties. It provides a high-precision benchmark for future EE computations and establishes a long-missing link between exactly solvable limits and strongly correlated regimes in $(2+1)d$ dimensions.

II. RESULTS

We directly start with explaining the main results of the paper: our model design (Sec. II A), and then our PQC results of the phase diagram (Sec. II B) and the computed EE along the parameter path from Ising to Gaussian QCPs, to monitor the changes of the universal corner log-coefficients (Sec. II C). The detailed explanation of the analytic computation at the Gaussian fixed point and our algorithmic advancements of *Bubble basis* PQC and the superior EE computation therein, will be given in the next section.

A. From Ising to Gaussian at (2+1)d

The Hamiltonian of a TFIM on a square lattice, augmented with a four-body K interaction term, is given as

$$H = -J \sum_{\langle i,j \rangle} \sigma_i^z \sigma_j^z - h \sum_i \sigma_i^x - K \sum_{(a,d)(b,c)} (\sigma_a^z \sigma_d^z + \mathbf{I})(\sigma_b^z \sigma_c^z + \mathbf{I}), \quad (1)$$

where $\sigma = \{\sigma^x, \sigma^y, \sigma^z\}$ denotes the Pauli matrices, i labels a lattice site, and $\langle i, j \rangle$ denotes a nearest-neighbor pair of sites. The system has $N = L \times L$ sites in total, where L is the linear size. We consider the ferromagnetic case, set $J = 1$ as the energy unit, and take h to be the transverse-field strength. To realize the Gaussian fixed point, we consider a K -term into the TFIM where (a, d) and (b, c) denote two distinct bonds in a plaquette, as illustrated in the lower right inset of Fig. 1 (a).

According to the RG flow analysis provided in the Sec. I of Supplemental Material (SM) [28], at (2+1)d the turning of the K -term controls the value of the λ_4 -term in the field theory. When $\lambda_4 > 0$, turning the h/J corresponds to tune from $m^2 < 0$ to $m^2 > 0$ and the system experience a (2+1)d Ising QCP from ferromagnetic (FM) to paramagnetic (PM) phases. When $\lambda_4 < 0$, turning the h/J would generate a first order transition from FM to PM phases. The fine-tuned point of $\lambda_4 = 0$ will give rise to a Gaussian fixed point between the ferromagnetic and PM phases, as a function of h/J . Of course, the microscopic value of the K in the lattice model upon which the coupling constant λ_4 vanishes in the field theory is not known a priori, and that is why the unbiased QMC simulation is needed to determine the phase diagram in Fig. 1 (a) in the first place.

B. Phase Diagram

Fig. 2 (a), (d) and (g) show the analysis of the Binder cumulant $U_L = \frac{3}{2} \left(1 - \frac{\langle M_z^4 \rangle}{3 \langle M_z^2 \rangle^2} \right)$ for various values of the tuning parameter h at $K = 5$, $K = 16.02$, and $K = 320$, with the linear system sizes from $L = 4$ up to $L = 64$. The Binder cumulants approach 1 at small h and 0 at large h for all three K values, indicating a transition from a FM to a PM phase with increasing h . The nature of this transition, however, depends on the value of K . For $K = 5$ and $K = 16.02$, the Binder cumulant exhibits behavior characteristic of a continuous phase transition. In contrast, for $K = 320$, the transition is first-order, as evidenced by the emergence of negative values in the Binder cumulant [29, 30] to the right of the critical point for $L > 10$.

To further classify the universality classes of the continuous transitions, we performed a finite-size scaling analysis. For the continuous transition at $K = 5$, the data collapse was successfully achieved using the (2+1)d Ising critical exponent (correlation length exponent $\nu = 0.63$), as illustrated in Fig. 2 (b), confirming that it belongs to the Ising universality class and give rise $h_c = 23.9(5)$. For $K = 16.02$, a satisfactory data collapse was obtained only when using Gaussian exponent (correlation length exponent $\nu = 1/2$), shown in Fig. 2 (e), indicating its affiliation with the Gaussian universality class,

and the corresponding $h_c = 67.57(4)$. For the first-order transition at $K = 320$, attempts to collapse the data using either (2+1)d Ising or Gaussian exponents were unsuccessful (Fig. 2 (h) and (i)), which provides additional support for the first-order nature of the transition at this point. The very large value of K was selected specifically to distance the system from the Gaussian critical point, thereby cleanly isolating and demonstrating the characteristic first-order behavior.

We also set the position of the QCP (h_c) and the correlation length exponent (ν) as free parameters and record the coefficient of determination, R^2 , of the data collapse with each set of (h_c, ν) such that the optimized collapse can be determined with the optimized choice of the (h_c, ν) for different K cuts. The corresponding heatmap are shown in Fig. 2 (c) and (f). It is obvious from these analyses that for $K = 5$, the optimized data collapse can be obtained only when the $\nu = 0.63(5)$ which correspond to the (2+1)d Ising QCP, whereas for $K = 16.02$, the optimized data collapse can be only be obtained when $\nu = 0.52(5)$, which correspond to the Gaussian QCP.

The raw data presented in Fig. 2 were acquired using the PQMC method in the σ_z basis. This choice was made because, as will be discussed in the Secs. III B and III C, the σ_z basis PQMC demonstrates better efficiency than bubble basis PQMC for calculating standard physical observables such as energy, magnetization, and the Binder cumulant, but worse efficiency in computing the exponential observables [2], such as EE and free energy.

C. Universal terms in the EE

In a finite-size system, the EE is found to adhere to the area law, expressed as

$$S_2^A = a l_A - s \ln(l_A) + c, \quad (2)$$

where l_A is the boundary length of the entanglement region (typically proportional to the linear system size L , as illustrated in the inset of Fig. 1 (a)), a is a non-universal coefficient associated with the area-law term, s is a universal coefficient quantifying the subleading logarithmic correction, which depends on the presence of sharp corners in the entanglement region and the ground state properties, and c is a constant.

At the Gaussian point, the logarithmic correction arising from sharp corners is well-established and considered exactly solvable, as discussed in Sec. III A. For the entanglement region shown in the inset of Fig. 1 (a), which contains four 90° corners, the universal coefficient of this logarithmic correction at the Gaussian point is known to be $s = 0.02567$ [4, 5] (cf. Fig. 3).

In this study, we employ the bubble basis PQMC method to compute the EE of the TFIM, augmented with a K term, precisely at its critical point (K_c, h_c). The entropy calculation utilizes the advanced incremental method [1, 17], enhanced further by the subtracted corner entanglement entropy (SCEE) technique [3, 15, 18]. The SCEE technique is specifically designed to isolate the universal log-coefficients originating from sharp corners on the entanglement boundary during one

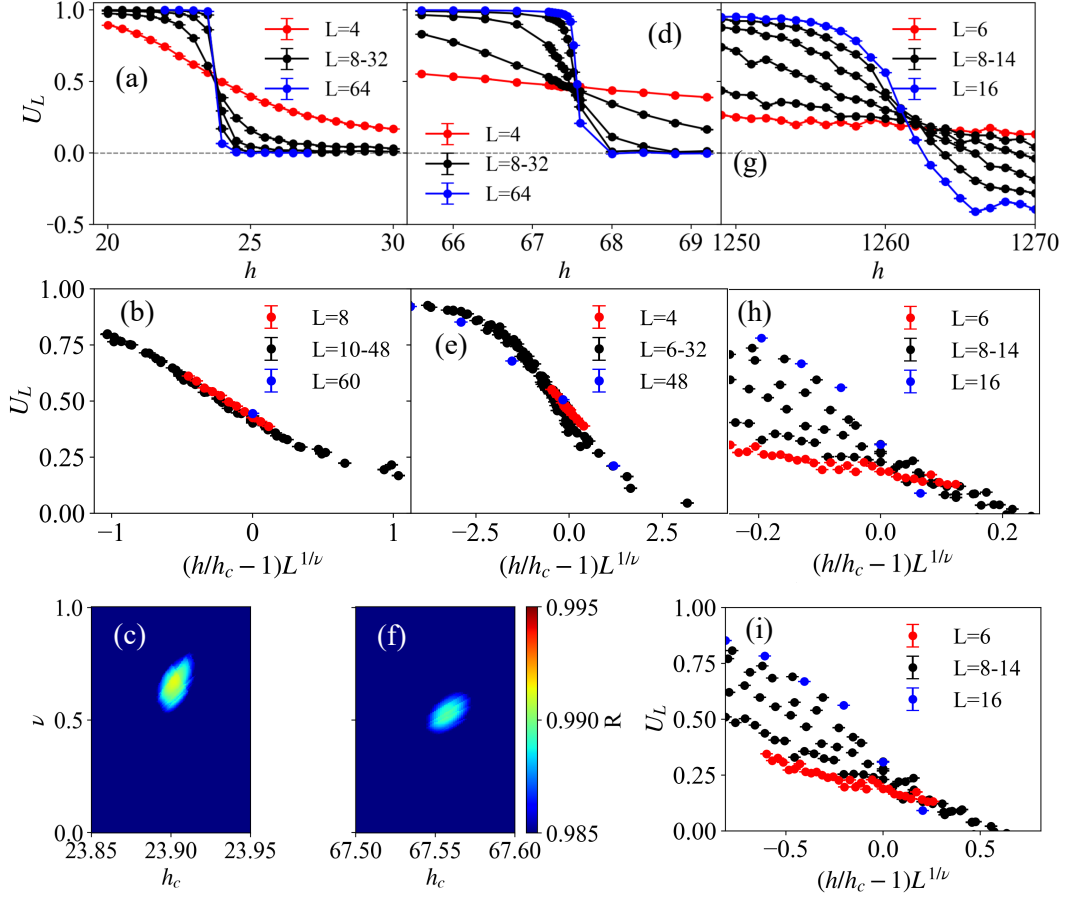


FIG. 2. **Finite-size scaling analysis of the phase transitions driven by transverse field h at different values of parameter K .** (a-c) $K = 5$: (a) Binder cumulant U_L as a function of h for different system sizes up to $L = 64$. The crossing point of the curves determines the critical field $h_c^{K=5} = 23.9(5)$. (b) Data collapse of U_L using the finite-size scaling relation $U_L \sim (h/h_c - 1)L^{1/\nu}$ with the 3D Ising universality critical exponent $\nu = 0.63$. The high quality of the collapse confirms a continuous phase transition. (c) Heat map of the R statistic for the data collapse, evaluated over a range of ν and h_c values. The optimal region of high R aligns with $\nu = 0.63$, providing further evidence that the continuous phase transition belongs to the 3D Ising universality. (d-f) $K = 16.02$: (d) Binder cumulant U_L versus h for different L up to 64. The intersection point identifies $h_c^{K=16.02} = 67.57(4)$. (e) Data collapse of U_L using the Gaussian (free) universality critical exponent $\nu = 0.5$, indicating a continuous phase transition belonging to this class. (f) Heat map based on the R criterion for the finite-size scaling relation, exploring different values of ν and h_c . The bright region confirming the best data collapse includes $\nu = 0.5$, consistent with the Gaussian universality. (g-i) $K = 320$: (g) Binder cumulant U_L as a function of h for different L up to 16. The emergence of negative U_L values for $L = 12$ and $L = 16$ at certain values of h is a signature of a first-order phase transition. (h) Attempted data collapse of U_L using the 3D Ising critical exponent ($\nu = 0.63$) fails. (i) Attempted data collapse using the Gaussian critical exponent ($\nu = 0.5$) also fails. The poor quality of both collapse attempts provides additional evidence for a first-order phase transition at this parameter.

QMC simulation. These coefficients are vital for characterizing quantum criticalities and their underlying conformal field theories. This is achieved by calculating the difference between the EEs of two strategically chosen subregions, A_1 and A_2 , within the same system, as depicted in the upper inset of Fig. 1 (a). Subregion A_1 possesses a smooth boundary, and its EE follows the form

$$S_2^{A_1} = al_{A_1} + \gamma_1, \quad (3)$$

while subregion A_2 , which contains corners, exhibits an EE given by

$$S_2^{A_2} = al_{A_2} - s \ln l_{A_2} + \gamma_2. \quad (4)$$

The subregions are selected such that their boundary lengths are equal: $l_{A_1} = l_{A_2} = 2L$. The SCEE is then defined as the difference between $S_2^{A_1}$ and $S_2^{A_2}$:

$$S_s = S_2^{A_1} - S_2^{A_2} = s \ln L + \gamma, \quad (5)$$

where $\gamma = \gamma_1 - \gamma_2$. This differential approach inherently cancels the dominant, non-universal area-law term in the entanglement entropy. Consequently, the universal corner contribution emerges as the leading term in the scaling analysis, enabling its precise and straightforward extraction. Moreover, the quantity S_s can be obtained directly in the QMC simulation. This approach is more efficient and yields better precision than first calculating $S_2^{A_1}$ and $S_2^{A_2}$ separately and then

subtracting them, as it avoids the accumulation of errors from the subtraction operation, which was performed in previous QMC works [24–27].

Fig. 1 (b) demonstrate the S_s versus $\ln(L)$ along the critical boundary in Fig. 1 (a) for various K values. L_{\max} takes values of 40, 38, 38, 36, 14, and 14 for $K = 0, 5, 10, K_c, 160$, and 320, respectively. We found as L increases, the expected $S_s \sim s \ln(L)$ behavior (Eq. (5)) manifests, and for $K = 0, 5, 10 < K_c$, i.e., the (2+1)d Ising QCPs, the curves are all parallel (although their intercepts are different) which implies the equal value of the universal log-coefficient s . Then in Fig. 1 (d), (e) and (f), we performed the extrapolation of s by gradually removing the smallest system size L_{\min} in the fitting process, and one sees that s of there curves nicely yield the $s = 0.020(1)$. We note that for all extrapolations, the process is stopped once the two smallest values of $1/L_{\min}$ converge. The final converged slope is obtained by averaging the results from the last two points.

At $K = K_c$, i.e., at the Gaussian fixed point, it is interesting to see that the slope in Fig. 1 (b) is distinctively different from those Ising QCPs. Here we put the analytic value of $s = 0.02567$ by hand in the figure, and one sees the data follow the expectation perfectly. Moreover, in Fig. 1 (g), we performed the same $1/L_{\min}$ extrapolation and found that converged $s = 0.025(1)$ steadily land at the theoretical value for the Gaussian fixed point (red dashed line). We emphasize that without our bubble PQMC and the incremental SWAP implementation in this basis, and the SCEE cancellation of the area-law term in QMC sampling, the 1/1000 difference of the $s = 0.020(1)$ for (2+1)d Ising QCP and the $s = 0.025(1)$ for (2+1)d Gaussian QCP, were not possible with conventional computations.

For $K = 160, 320 > K_c$, the system exhibits a first-order phase transition, characterized by the coexistence of PM and FM phases. Our numerical results demonstrate that the universal corner coefficient s vanishes, as shown in Fig. 1(c) and its extrapolation in Fig. 1(h). This observation can be understood from the superposition of the contributions from the PM and FM phases, both of which are product states with gapped spectra and expected to have vanishing individual corner coefficients. Consequently, at the first-order transition point, the overall value is found to be $s = 0$.

The summary of the converged universal corner log-term along the Ising to Gaussian and eventually 1st order phase boundary, is given in Fig. 1 (c).

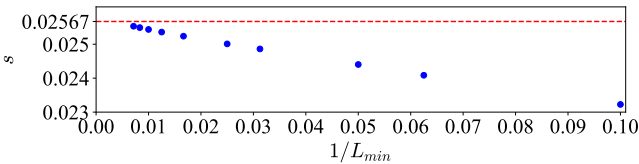


FIG. 3. **Universal corner term in a free theory.** In 2d square lattice with the entanglement area having four 90° corners, one can compute the universal term s in Eq. (10) and extrapolate the value with the inverse linear size of the region $1/L_{\min}$, the extrapolated value is $s = 0.02567$. The red dashed line is the reference value from literature [4, 5].

III. ANALYTIC RESULTS AND ALGORITHMIC ADVANCES OF THE BUBBLE PQMC

We now explain the analytic computation of the universal corner EE at the Gaussian fixed point (Sec. III A), and algorithmic advancements of *bubble basis* PQMC (Sec. III B) and the superior incremental SWAP EE computation in the bubble basis (Sec. III C), over the previous σ^z -basis.

A. EE for free theory in a lattice

Following Refs. [4, 5, 31], here we perform a calculation of the universal corner log-term in EE for a free scalar theory on a square lattice. To this end, we evaluate the Rényi entropy for a massless real scalar with the Hamiltonian

$$\begin{aligned} H &= \frac{1}{2} \sum_i \pi_i^2 + \frac{1}{2} \sum_{\langle i,j \rangle} (\phi_i - \phi_j)^2 \\ &= \frac{1}{2} \sum_i \pi_i^2 + \frac{1}{2} \sum_{i,j} \phi_i M_{i,j} \phi_j, \end{aligned} \quad (6)$$

where ϕ_i and π_i are the free boson field and its canonical momentum, with the canonical commutation relation $[\phi_i, \pi_j] = i\delta_{i,j}$. The model is placed on a $L \times L$ lattice, and M is the $N \times N$ (with $N = L^2$) lattice Laplacian matrix. In order to avoid zero mode, we impose anti-periodic boundary condition for ϕ in the y direction (and periodic in x). From the Hamiltonian, we find the following correlators

$$X_{ij} = \langle \phi_i \phi_j \rangle = \frac{1}{2} (M^{-1/2})_{ij} \quad (7)$$

$$P_{ij} = \langle \pi_i \pi_j \rangle = \frac{1}{2} (M^{1/2})_{ij}. \quad (8)$$

The entanglement entropy can be obtained using the following method. Denote the restriction of X to a region A by X_A (and similarly define P_A). Diagonalize the matrix $\sqrt{X_A P_A}$, with eigenvalues ϵ_n . The 2nd Rényi EE is given by

$$S_2^A = - \sum_n \ln \left(\left(\epsilon_n + \frac{1}{2} \right)^2 - \left(\epsilon_n - \frac{1}{2} \right)^2 \right) = - \sum_n \ln(2\epsilon_n). \quad (9)$$

In order to cancel the leading perimeter term, we also employ the SCEE scheme and take the difference between them:

$$S_s = S_2^{A_1}(L) - S_2^{A_2}(L) = s \ln L + \gamma + O(1/L). \quad (10)$$

We gradually skip the smaller system sizes in the fitting, i.e., by throwing away linear size $L < L_{\min}$, the converged universal corner term $s = 0.02567$ for four 90° corners, is obtained as shown in Fig. 3. This is the reference value we used to compare the s from QMC simulation at the (2+1)d Ising and Gaussian QCPs, in fact, our Gaussian QCP from PQMC simulation at $K = K_c$ indeed recovers this number, as shown in Fig. 1 (b), (c) and (g).

B. Projector quantum Monte Carlo in Bubble basis

The PQMC method for bosonic/spin system was introduced by Sandvik in 2005 for SU(2) quantum spins using the valence-bond basis [32]; later, a combined spin and valence-bond basis for SU(2) quantum spins was proposed to enable more efficient simulations [33]. In 2013, Inglis and Melko adapted PQMC to the TFIM in the σ_z basis, enabling the calculation of the Rényi EE in such basis [24].

In the ground state, the expectation value of an operator O is

$$\langle O \rangle = \frac{1}{Z} \langle \psi^0 | O | \psi^0 \rangle, \quad (11)$$

where $|\psi^0\rangle$ is the unnormalized ground state wavefunction and $Z = \langle \psi^0 | \psi^0 \rangle$ is the normalization. In PQMC framework, $|\psi^0\rangle$ is estimated by a projection procedure on a *trial* state $|\alpha^0\rangle$ as

$$(-H)^m |\alpha^0\rangle \rightarrow |\psi^0\rangle, \text{ as } m \rightarrow \infty.$$

To understand this projection procedure, one can write $|\alpha^0\rangle$ as linear superposition of energy eigenstates of Hamiltonian $|\alpha^0\rangle = \sum_i c_i |\psi^i\rangle$, then

$$(-H)^m |\alpha^0\rangle = (-E_0)^m \left[c_0 |\psi^0\rangle + c_1 \left(\frac{E_1}{E_0} \right)^m |\psi^1\rangle \cdots \right], \quad (12)$$

where we assume that E_0 has the largest magnitude among all E_i and this can be ensured by adding a sufficiently large negative constant to H . Then, for large enough m , one can obtain $\langle O \rangle$ as,

$$\langle O \rangle = \frac{\langle \alpha_l^0 | (-H)^m O (-H)^m | \alpha_r^0 \rangle}{\langle \alpha_l^0 | (-H)^m (-H)^m | \alpha_r^0 \rangle}, \quad (13)$$

where $\langle \alpha_l^0 |$ and $|\alpha_r^0\rangle$ represent the left and right trial wavefunctions, they may be identical or distinct as there is no need for orthogonalisation.

To introduce the PQMC sampling, we rewrite the Hamiltonian (up to an additive constant) as,

$$H = -J \sum_{N_J} H_J - h \sum_{N_h} H_h - K \sum_{N_K} H_K, \quad (14)$$

where $H_J = (\sigma_i^z \sigma_j^z + \mathbf{I})$ is the bond operator and $H_h = (\sigma_i^+ + \sigma_i^- + \mathbf{I})$ is the site operator with $\sigma^+ = (\sigma^x + i\sigma^y)/2$ and $\sigma^- = (\sigma^x - i\sigma^y)/2$, $H_K = (\sigma_a^z \sigma_d^z + \mathbf{I})(\sigma_b^z \sigma_c^z + \mathbf{I})$ represents the four-body operator, and \mathbf{I} the identity operator. For a 2D system, $N_J = 2N$ is the total number of bonds, $N_K = N$ and $N_h = N$.

We sample the operators H_a , with $a \in \{J, h, K\}$ by evaluating

$$\langle O \rangle = \frac{\sum_{\{c\}} \langle \alpha_l^0 | \prod_{i=1}^m H_{a_i} O \prod_{j=1}^m H_{a_j} | \alpha_r^0 \rangle}{\sum_{\{c\}} \langle \alpha_l^0 | \prod_{i=1}^m H_{a_i} \prod_{j=1}^m H_{a_j} | \alpha_r^0 \rangle} = \frac{\sum_{\{c\}} \mathcal{W}_c O_c}{\sum_{\{c\}} \mathcal{W}_c}, \quad (15)$$

where $c \equiv \{a_1, a_2, \dots, a_{2m}\}$ is a configuration representing a set of operators in $2m$ projection space, the configuration weight is given as

$$\mathcal{W}_c = \langle \alpha_l^0 | \prod_{i=1}^{2m} H_{a_i} | \alpha_r^0 \rangle, \quad (16)$$

and the estimator is

$$O_c = \langle \alpha_l^0 | \prod_{i=1}^m H_{a_i} O \prod_{j=1}^m H_{a_j} | \alpha_r^0 \rangle / \mathcal{W}_c. \quad (17)$$

In principle, the PQMC framework is basis-independent. In practice, however, the choice of basis is critical for constructing a trial wavefunction that, when acted upon by the operator H_a , avoids branching, and ensures the weights \mathcal{W}_c remain non-negative thereby circumventing the sign problem. As demonstrated in Ref. [24], the σ_z basis meets these requirements, leading to an algorithm with overall computational complexity scaling as $O(m)$. However, precise calculation of the Rényi EE, which is recognized as an exponential observable [2], often necessitates specialized techniques like the incremental approach to overcome severe statistical instability in direct sampling [1, 2, 17]. Applying this incremental technique within the conventional σ_z basis PQMC framework for computing the EE of the TFIM entails a significant increase in computational complexity. As we analyze below, the total cost escalates disadvantageously to $O(m^2 + mN)$, which severely restricts the system sizes for which reliable EE analysis is feasible.

To enable accurate EE calculation for considerably larger systems, thereby allowing more robust finite-size scaling and credible revelation of universal properties, we introduce a new PQMC framework formulated in a *bubble basis*. As shown below, when combined with the incremental technique, our bubble basis PQMC substantially reduces the computational overhead to $O(mP)$, where P scales as a power-law in the linear system size L in the FM phase and at the critical point, but remains $O(1)$ in the PM phase, as shown in Fig. 7. This improvement dramatically enhances the efficiency of precise EE computations.

As illustrated in Fig. 4, a state $|\alpha^0\rangle$ in bubble basis is employed as the trial wave function. The term “bubble” is used because, when visualizing the evolution of the state, the loops formed by different lattice sites resemble bubbles floating in the configuration space. Within a single bubble, all sites share the same spin orientation, either all up or all down. In other words, a bubble state is a superposition of σ^z product states. For example, for the right trial wave function in Fig. 5, in a four-sites system with four bubbles, we have $|\alpha_R^0\rangle = |(\uparrow + \downarrow)(\uparrow + \downarrow)(\uparrow + \downarrow)(\uparrow + \downarrow)\rangle$. It is straightforward to verify that the application of a bond operator H_J , a site operator H_h , or a four-body operator H_K to a bubble state results in another bubble state, with no branching occurring, as shown in panels (a)-(h) in Fig. 4.

It is straightforward to verify that the overlap of two bubble states is

$$\langle \alpha | \beta \rangle = 2^{N_B}, \quad (18)$$

where N_B is the number of link-bubbles formed by connecting the bubbles between $\langle \alpha |$ and $|\beta \rangle$ via their one-to-one site corresponding nodes and an example is shown in Fig. 6. To estimate the observable $\langle \alpha | O | \beta \rangle$, one can first propagate $O | \beta \rangle$ to a new bubble state $|\gamma \rangle$ then calculate the overlap $\langle \alpha | \gamma \rangle$. Alternatively, one can revert to the σ^z basis, as defined for bubble states.

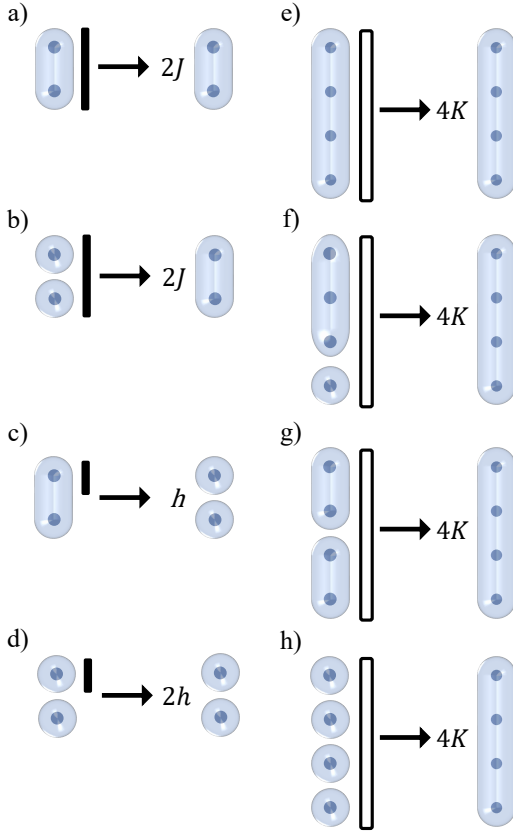


FIG. 4. **Illustration of the bubble basis and its operator evolution.** The H_K acts on a square of four spins, but for illustration purposes, it is compressed and shown as a one-dimensional bar here. a) and b) show the action of H_J , c) and d) show the action of H_h and e) - h) show the action of H_K on the bubble basis. After acting the operators on the basis, they would give different constants as described in Eq. (16) and these constants are also shown next to the bubbles.

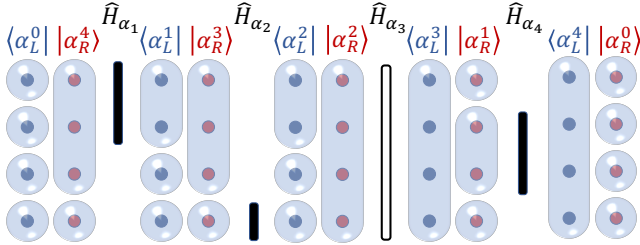


FIG. 5. **Propagation of the operators.** This graph gives a pictorial representation of Eq. (19). It shows a configuration with $m = 2$ and the operators $H_{\alpha_1} - H_{\alpha_4}$ are H_J, H_h, H_k and H_j respectively. The actions of different operators on the bubble basis are illustrated in Fig. 1, and the constants are neglected here.

To update a configuration c to c' according to the Metropolis algorithm within PQMC, calculating the configuration weight ratio $\mathcal{W}_{c'}/\mathcal{W}_c$ is a key step. This ratio determines the acceptance probability for the proposed move. A direct calculation of the individual weights \mathcal{W}_c and $\mathcal{W}_{c'}$ using the explicit Eq. (16) typically involves computations for projec-

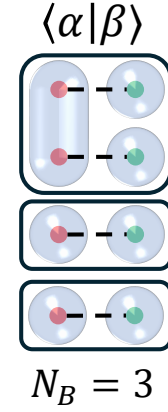


FIG. 6. **Illustration of the overlap of bubble basis.** Here $\langle \alpha | = \langle (\uparrow\uparrow + \downarrow\downarrow)(\uparrow + \downarrow)(\uparrow + \downarrow) |$ and $|\beta\rangle = |(\uparrow + \downarrow)(\uparrow + \downarrow)(\uparrow + \downarrow)(\uparrow + \downarrow)\rangle$. The dash lines represent the one-to-one site corresponding notes. In this example, the black solid lines are the link-bubbles and the number of independent link-bubbles is $N_B = 3$.

tion evolution and the state overlaps. For a local update of the configuration—where only a single operator H_{a_j} is changed to H'_{a_j} at the j -th projection time slice, leaving all other operators unchanged—this direct approach can lead to a computational complexity of $O(m + N)$. Here m and N come from projection evolution and the state overlaps, separately. To achieve a more efficient calculation, the recently developed propagating update strategy by us [1] is used.

The key idea of the propagating update strategy is that, for a local update, Eq. (16) can be reformulated as,

$$\left\langle \alpha_l^0 \left| \prod_{i=1}^{2m} H_{a_i} \right| \alpha_r^0 \right\rangle = 2^{(n_l^{j-1} + n_r^{2m-j})} \left\langle \alpha_l^{j-1} | H_{a_j} | \alpha_r^{2m-j} \right\rangle, \quad (19)$$

where the value of n_l^{j-1} is determined by the sequence of operator actions encountered during the projector process $\langle \alpha_l^{j-1} |$, which evolves from $\langle \alpha_l^0 | \prod_{i=1}^{j-1} H_{a_i}$, as illustrated in Fig. 5. According to Fig. 4, each operator action corresponding to panels (a), (b), and (d) increments n_l^{j-1} by 1. Actions represented by panel (c) contribute 0, while those shown in panels (e) to (h) increment n_l^{j-1} by 2. Conversely, n_r^{2m-j} represents an analogous count for the process $|\alpha_r^{2m-j}\rangle$, which evolves from $\prod_{i=j+1}^{2m} H_{a_i} |\alpha_r^0\rangle$.

For a local update from H_{a_j} to H'_{a_j} , the weight ratio can be calculated straightforwardly as

$$\frac{\mathcal{W}_{c'}}{\mathcal{W}_c} = \frac{\langle \alpha_l^{j-1} | H'_{a_j} | \alpha_r^{2m-j} \rangle}{\langle \alpha_l^{j-1} | H_{a_j} | \alpha_r^{2m-j} \rangle}. \quad (20)$$

Since this approach avoids recomputing the entire propagation, the computational complexity for a local update is reduced from $O(m + N)$ to $O(N)$, where $O(N)$ arises from the overlap calculation. The evaluation of the ratio can be further accelerated by introducing an auxiliary state, leading to the

reformulated expression,

$$\frac{\mathcal{W}_c}{\mathcal{W}_c} = \frac{\langle \alpha_l^{j-1} | H_{a_j} | \alpha_r^{2m-j} \rangle / \langle \alpha_l^{j-1} | \alpha_r^{2m-j} \rangle}{\langle \alpha_l^{j-1} | H_{a_j} | \alpha_r^{2m-j} \rangle / \langle \alpha_l^{j-1} | \alpha_r^{2m-j} \rangle}. \quad (21)$$

As illustrated in Fig. 4, the action of a bond operator H_j either merges two bubbles into one or leaves a bubble unchanged. If we express the overlap as $\langle \alpha_l^{j-1} | H_{a_j} | \alpha_r^{2m-j} \rangle = 2^{N'_B}$ and $\langle \alpha_l^{j-1} | \alpha_r^{2m-j} \rangle = 2^{N_B}$, then the difference $N'_B - N_B$ is either -1 or 0 . Consequently, $\langle \alpha_l^{j-1} | H_{a_j} | \alpha_r^{2m-j} \rangle / \langle \alpha_l^{j-1} | \alpha_r^{2m-j} \rangle$ takes a value of 2^{-1} or 2^0 when H_{a_j} represents a bond operator. Similarly, a site operator H_h either splits one bubble into two or leaves it unchanged, resulting in possible values of 2^1 or 2^0 for $\langle \alpha_l^{j-1} | H_{a_j} | \alpha_r^{2m-j} \rangle / \langle \alpha_l^{j-1} | \alpha_r^{2m-j} \rangle$ when H_{a_j} represents a site operator. A four-body K -term operator can be treated as the product of two bond operators. Furthermore, determining the value of $N'_B - N_B$ only requires consideration of the link-bubbles that contain the sites involved in the operator. Therefore, the computational complexity of the weight ratio calculation via the accelerated Eq. (21) can be expressed as $O(P)$, where P denotes the statistical average of the number of lattice sites within the link-bubbles connected to the operator being updated.

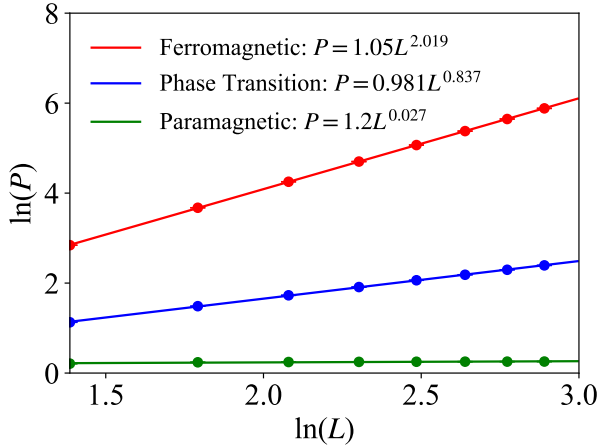


FIG. 7. **Complexity analysis of different phases at $K = 0$.** Inside the FM phase $P \sim L^2$, at the Ising QCP $P \sim L^{0.84}$ and inside the PM phase $P \sim L^{0.03}$ is almost a constant.

As illustrated in Fig. 7, P exhibits a power-law scaling with the system size L in the FM phase and at the critical point, while it remains $O(1)$ in the PM phase. In the FM phase, the tendency for all lattice sites to form a single collective “bubble” implies that the weight ratio calculation must account for the entire lattice. This is consistent with the observed scaling $P \sim L^2$, which equals the total number of lattice sites N . Conversely, in the PM phase, individual sites or small local clusters tend to form independent bubbles. Consequently, the value of P becomes a constant independent of L . Notably, at the critical point, numerical results indicate that P also follows a power-law scaling with L , but with a reduced exponent of

approximately 0.8. This leads to a significant computational speedup compared to the FM phase. When considering the full projection time slice, the total computational complexity of the PQMC method with the bubble basis is therefore $O(mP)$, where m is the number of time slices.

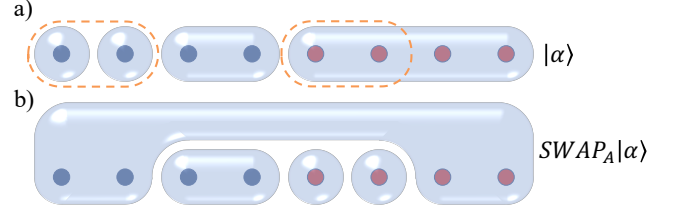


FIG. 8. **SWAP operator actions on bubble basis.** An eight-site chain with two interacting copies (blue and red color sites) before (a) and after (b) $SWAP_A$. The green dotted line circles the entangled region A. The bubbles in the graph follow the same definition as in the main text.

We have successfully applied the developed PQMC algorithm in the bubble basis to compute the phase diagram of the transverse field Ising model, as shown in Sec. III of SM [28]. Our results indicate that a continuous phase transition from a FM to a PM state occurs at a critical field of $h_c = 3.044(2)$. The critical exponents obtained numerically demonstrate that this phase transition belongs to the (2+1)d Ising universality class, which is consistent with previous literature [34–36].

C. EE computation in the Bubble PQMC

As discussed above, the total computational complexity of PQMC with the bubble basis is $O(mP)$. In the PM phase, $P \sim 1$, whereas in the FM phase and at QMC, $P \sim L^\alpha$. In our case, $\alpha = 2$ in the FM phase and $\alpha = 0.8$ at QCP (cf. Fig. 7). The PQMC with the σ_z basis developed in Ref. [24] has computational complexity $O(m)$ across all phases. Consequently, our method is as efficient as the σ_z basis PQMC in the PM phase, but it is less efficient in the FM phase and at the QCP. However, for computing the Rényi EE, our method offers a significant efficiency advantage. We reduce the $O(m^2 + mN)$ complexity for EE computation in σ_z basis to $O(mP)$ in bubble basis, as we explain below.

The 2nd Rényi EE can be estimated by the expectation value of $SWAP_A$ operator using a replica trick in QMC [24, 37, 38],

$$e^{-S_2^A} = \frac{\sum_{\{c_1\}, \{c_2\}} \mathcal{W}_{12}(SWAP_A / \mathcal{W}_{12})}{\sum_{\{c_1\}, \{c_2\}} \mathcal{W}_{12}} \quad (22)$$

where $\mathcal{W}_{12} = \mathcal{W}_{c_1} \mathcal{W}_{c_2}$ is the weight product of two replicas, A is the entanglement region as shown in the inset of Fig. 1 (a) and

$$SWAP_A = \langle \alpha_{l,12}^0 | \prod_{i=1}^m H_{a_i,1} H_{a_i,2} \widehat{SWAP}_A \prod_{j=1}^m H_{a_j,1} H_{a_j,2} | \alpha_{r,12}^0 \rangle, \quad (23)$$

where $\langle \alpha_{l,12}^0 | = \langle \alpha_{l,1}^0 | \otimes \langle \alpha_{l,2}^0 |$ and $|\alpha_{r,12}^0\rangle = |\alpha_{r,1}^0\rangle \otimes |\alpha_{r,2}^0\rangle$ are the left and right trail wavefunctions of a system containing two replicas, respectively.

Recent studies have established that EE is an exponential observable [1, 2, 17], and directly evaluating SWAP_A is plagued by convergence problems. To overcome these issues, the power incremental algorithm provides an elegant and straightforward operational approach [1, 17]. Rather than estimating SWAP_A directly, one should compute it in an incremental form

$$e^{-S_2^A} = \frac{Z(1)}{Z(0)} \frac{Z(2)}{Z(1)} \cdots \frac{Z(k+1)}{Z(k)} \cdots \frac{Z(n)}{Z(n-1)}, \quad (24)$$

where $Z(k) = \sum_{\{c_1\}, \{c_2\}} \mathcal{W}_{12}(\text{SWAP}_A / \mathcal{W}_{12})^{k/n}$. Here integer k indexes the k -th increment out of a total of n increments. The value of n can be quantitatively determined based on the scaling of $\log(\text{SWAP}_A)$. With $Z(0) = \sum_{\{c_1\}, \{c_2\}} \mathcal{W}_{12}$ and $Z(n) = \sum_{\{c_1\}, \{c_2\}} \mathcal{W}_{12}(\text{SWAP}_A / \mathcal{W}_{12})$, the final product naturally yields the definition of the 2nd Rényi EE. Each incremental ratio can then be evaluated in parallel with PQMC as follows

$$\frac{Z(k+1)}{Z(k)} = \frac{\sum_{\{c_1\}, \{c_2\}} \mathcal{W}_{12}^{1-k/n} (\text{SWAP}_A)^{k/n} (\text{SWAP}_A / \mathcal{W}_{12})^{1/n}}{\sum_{\{c_1\}, \{c_2\}} \mathcal{W}_{12}^{1-k/n} (\text{SWAP}_A)^{k/n}}. \quad (25)$$

To evaluate the expectation value of $\frac{Z(k+1)}{Z(k)}$, for the TFIM within a specific configuration using a σ^z -basis PQMC simulation, one must first construct clusters for the off-diagonal update. The value is then determined by counting the number of independent clusters that cross the central time-slice, as detailed in Ref. [24]. When calculating the incremental ratio $\frac{Z(k+1)}{Z(k)}$ within this σ^z -basis framework, the swap operator contributes to the update weight. Consequently, for every local update at any projection time slice, it is necessary to perform a projection evolution to the middle time-slice and reconstruct the clusters to count the crossing clusters. This process results in a total computational complexity of $O(m^2 + mN)$, which is highly inefficient.

In contrast, the bubble basis PQMC approach offers a significant advantage. The action of the SWAP operator on a bubble state generates a new, well-defined bubble state, as illustrated in Fig. 8. This property allows for the use of a propagating update strategy based on Eq. (21), which can be directly applied to the SWAP operator during updates. As a result, the total computational complexity for obtaining $\frac{Z(k+1)}{Z(k)}$ remains $O(mP)$, making the bubble basis PQMC method significantly faster than the σ^z -basis approach.

IV. DISCUSSION

Based on the description in Secs. II and III, as for the two questions that were asked in the introduction, that,

- it is difficult to access the intensive and subleading universal term of corner coefficient from the extensive results of the EE computation,

- there exists no previous attempt that within one QMC computation, the analytically known results of these universal terms can be recovered consistently and then extend the computation to the strongly coupling regime, at $(2+1)d$,

we believe these two questions are solved satisfactorily in this work.

By designing a lattice model that hosts QCPs from $(2+1)d$ Ising to Gaussian, and by efficiently computing the EE with the incremental SWAP method such that the leading area-law contributions are eliminated within one simulation and the sub-leading logarithmic term is promoted to the leading term. We obtained the precise quantitative values of the universal corner log-coefficient in EE for the $(2+1)d$ Ising and Gaussian QCPs. We find that these two universalities are distinguishably different in their universal term of EE, through our high precision measurements, of 0.020(1) for the former and 0.025(1) for the latter for four 90° corners of the entangle area. The exact matching with the analytic results [4, 5] at the Gaussian QCP, implies that our Ising value is by far the most accurate one among all the previous attempts.

The significance of this work can be appreciated in a broader perspective. Our computation scheme gives the future QMC computation of the EE a solid foundation, and the further methodology developments, either in the projector QMC or path-integral QMC, can now use the present results and computational complexity as the necessary benchmark to evaluate the performance of their simulations.

Looking ahead, it is now the time to extend such a comparison between the analytic results at Gaussian CFT and the numerical results from large-scale computation to other entanglement measurements, such as multipartite entanglement [39–41], quantum Fisher information [42–44] and even quantum conditional mutual information for mixed state [45]. With the hope that at $(2+1)$ dimension or higher, these entanglement properties can bridge the fundamental entanglement concepts from precise analytic calculation for often-time weakly interacting systems, to practical model computations for strongly correlated systems and eventually applications to realistic experiments for quantum materials. In this way, exotic quantum critical points and emerging quantum many-body phases, and their associated theory, computation, and experimental verification, could be expected to unite from the entanglement perspective.

ACKNOWLEDGMENTS

We thank Cenke Xu and Meng Cheng for inspiring discussions on understanding the EE computation results over the years. We are particularly grateful to Meng Cheng for introducing the method to calculate EE following Refs. [4, 5, 31], and for sharing the data he obtained in Sec. III A. We acknowledge the support from the Research Grants Council (RGC) of Hong Kong (Project Nos. 17309822, C7037-22GF, 17302223, 17301924), the ANR/RGC Joint Research Scheme

sponsored by RGC of Hong Kong and French National Research Agency (Project No. A_HKU703/22). YDL acknowledges support from National Natural Science Foundation of China (Grant No. 12404282), YDL and ZYM acknowledge support from General Program of the Guangdong Natural Science Foundation (Grant No. 2025A1515010337). We thank HPC2021 system under the Information Technology Services at the University of Hong Kong, as well as the Beijing Paratera

Tech Corp., Ltd [46] for providing HPC resources that have contributed to the research results reported within this paper. The authors gratefully acknowledge the computing time made available to them on the high-performance computer Barnard at the NHR Center of TU Dresden. This center is jointly supported by the Federal Ministry of Education and Research and the state governments participating in the National High-Performance Computing (NHR) joint funding program [47].

-
- [1] X. Zhou, Z. Y. Meng, Y. Qi, and Y. Da Liao, Incremental SWAP operator for entanglement entropy: Application for exponential observables in quantum Monte Carlo simulation, *Phys. Rev. B* **109**, 165106 (2024).
- [2] X. Zhang, G. Pan, B.-B. Chen, K. Sun, and Z. Y. Meng, Integral algorithm of exponential observables for interacting fermions in quantum Monte Carlo simulations, *Phys. Rev. B* **109**, 205147 (2024).
- [3] Y. Da Liao, M. Song, J. Zhao, and Z. Y. Meng, Extracting universal corner entanglement entropy during the quantum Monte Carlo simulation, *Phys. Rev. B* **110**, 235111 (2024).
- [4] H. Casini and M. Huerta, Universal terms for the entanglement entropy in 2+1 dimensions, *Nuclear Physics B* **764**, 183 (2007).
- [5] J. Helmes, L. E. Hayward Sierens, A. Chandran, W. Witczak-Krempa, and R. G. Melko, Universal corner entanglement of Dirac fermions and gapless bosons from the continuum to the lattice, *Phys. Rev. B* **94**, 125142 (2016).
- [6] A. Einstein, B. Podolsky, and N. Rosen, Can Quantum-Mechanical Description of Physical Reality Be Considered Complete?, *Phys. Rev.* **47**, 777 (1935).
- [7] J. S. Bell, On the Einstein Podolsky Rosen paradox, *Physique Physique Fizika* **1**, 195 (1964).
- [8] J. F. Clauser, M. A. Horne, A. Shimony, and R. A. Holt, Proposed Experiment to Test Local Hidden-Variable Theories, *Phys. Rev. Lett.* **23**, 880 (1969).
- [9] V. Vedral, Quantifying entanglement in macroscopic systems, *Nature* **453**, 1004 (2008).
- [10] L. Amico, R. Fazio, A. Osterloh, and V. Vedral, Entanglement in many-body systems, *Reviews of modern physics* **80**, 517 (2008).
- [11] N. Laflorencie, Quantum entanglement in condensed matter systems, *Physics Reports* **646**, 1 (2016).
- [12] S. V. Isakov, M. B. Hastings, and R. G. Melko, Topological entanglement entropy of a Bose-Hubbard spin liquid, *Nature Physics* **7**, 772 (2011).
- [13] J. D’Emidio, Entanglement Entropy from Nonequilibrium Work, *Phys. Rev. Lett.* **124**, 110602 (2020).
- [14] J. Zhao, Y.-C. Wang, Z. Yan, M. Cheng, and Z. Y. Meng, Scaling of Entanglement Entropy at Deconfined Quantum Criticality, *Phys. Rev. Lett.* **128**, 010601 (2022).
- [15] M. Song, J. Zhao, Z. Y. Meng, C. Xu, and M. Cheng, Extracting subleading corrections in entanglement entropy at quantum phase transitions, *SciPost Phys.* **17**, 010 (2024).
- [16] J. D’Emidio, R. Orús, N. Laflorencie, and F. de Juan, Universal Features of Entanglement Entropy in the Honeycomb Hubbard Model, *Phys. Rev. Lett.* **132**, 076502 (2024).
- [17] Y. D. Liao, Universal Term of Entanglement Entropy in the π -Flux Hubbard Model, *npj Quantum Information* **11**, 64 (2025).
- [18] M. Song, J. Zhao, M. Cheng, C. Xu, M. Scherer, L. Janssen, and Z. Y. Meng, Evolution of entanglement entropy at SU(N) deconfined quantum critical points, *Science Advances* **11**, eadr0634 (2025).
- [19] J. I. Cirac, D. Pérez-García, N. Schuch, and F. Verstraete, Matrix product states and projected entangled pair states: Concepts, symmetries, theorems, *Rev. Mod. Phys.* **93**, 045003 (2021).
- [20] M. Levin and X.-G. Wen, Detecting Topological Order in a Ground State Wave Function, *Phys. Rev. Lett.* **96**, 110405 (2006).
- [21] A. Kitaev and J. Preskill, Topological Entanglement Entropy, *Phys. Rev. Lett.* **96**, 110404 (2006).
- [22] J. Zhao, B.-B. Chen, Y.-C. Wang, Z. Yan, M. Cheng, and Z. Y. Meng, Measuring Rényi entanglement entropy with high efficiency and precision in quantum Monte Carlo simulations, *npj Quantum Materials* **7**, 69 (2022).
- [23] S. Whitsitt, W. Witczak-Krempa, and S. Sachdev, Entanglement entropy of the large N Wilson-Fisher conformal field theory, *Phys. Rev. B* **95**, 045148 (2017).
- [24] S. Inglis and R. G. Melko, Entanglement at a two-dimensional quantum critical point: a $T = 0$ projector quantum Monte Carlo study, *New Journal of Physics* **15**, 073048 (2013), publisher: IOP Publishing.
- [25] E. M. Stoudenmire, P. Gustainis, R. Johal, S. Wessel, and R. G. Melko, Corner contribution to the entanglement entropy of strongly interacting O(2) quantum critical systems in 2+1 dimensions, *Phys. Rev. B* **90**, 235106 (2014).
- [26] A. B. Kallin, E. M. Stoudenmire, P. Fendley, R. R. P. Singh, and R. G. Melko, Corner contribution to the entanglement entropy of an O(3) quantum critical point in 2 + 1 dimensions, *Journal of Statistical Mechanics: Theory and Experiment* **2014**, P06009 (2014).
- [27] J. Helmes and S. Wessel, Entanglement entropy scaling in the bilayer Heisenberg spin system, *Phys. Rev. B* **89**, 245120 (2014).
- [28] The Supplemental Material provides the details on the RG flow analysis from the Gaussian fixed point to the Ising CFT at (2+1)d, the non-equilibrium measurement of EE in the path-integral QMC, and the benchmark results of magnetisation across the Ising QCP between Bubble and Spin bases.
- [29] K. Binder, K. Vollmayr, H.-P. Deutsch, J. D. Reger, M. Scheucher, and D. P. Landau, Monte Carlo Methods for First Order Phase Transitions: Some Recent Progress, *International Journal of Modern Physics C* **03**, 1025 (1992).
- [30] K. Vollmayr, J. D. Reger, M. Scheucher, and K. Binder, Finite size effects at thermally-driven first order phase transitions: A phenomenological theory of the order parameter distribution, *Zeitschrift für Physik B Condensed Matter* **91**, 113 (1993).
- [31] I. Peschel, Calculation of reduced density matrices from correlation functions, *Journal of Physics A: Mathematical and General* **36**, L205 (2003).
- [32] A. W. Sandvik, Ground State Projection of Quantum Spin Systems in the Valence-Bond Basis, *Phys. Rev. Lett.* **95**, 207203

- (2005).
- [33] A. W. Sandvik and H. G. Evertz, Loop Updates for Variational and Projector Quantum Monte Carlo Simulations in the Valence-Bond Basis, *Physical Review B* **82**, 024407 (2010).
 - [34] P. Pfeuty and R. J. Elliott, The Ising model with a transverse field. II. Ground state properties, *Journal of Physics C: Solid State Physics* **4**, 2370 (1971).
 - [35] S. Hesselmann and S. Wessel, Thermal Ising transitions in the vicinity of two-dimensional quantum critical points, *Phys. Rev. B* **93**, 155157 (2016).
 - [36] X. Y. Xu, K. Sun, Y. Schattner, E. Berg, and Z. Y. Meng, Non-Fermi Liquid at (2+1)D Ferromagnetic Quantum Critical Point, *Phys. Rev. X* **7**, 031058 (2017).
 - [37] Pasquale Calabrese and John Cardy, Entanglement Entropy and Quantum Field Theory, *Journal of Statistical Mechanics: Theory and Experiment* **2004**, P06002 (2004).
 - [38] M. B. Hastings, I. González, A. B. Kallin, and R. G. Melko, Measuring Renyi Entanglement Entropy in Quantum Monte Carlo Simulations, *Physical Review Letters* **104**, 157201 (2010).
 - [39] T.-T. Wang, M. Song, L. Lyu, W. Witczak-Krempa, and Z. Y. Meng, Entanglement microscopy and tomography in many-body systems, *Nature Communications* **16**, 96 (2025).
 - [40] L. Lyu, M. Song, T.-T. Wang, Z. Y. Meng, and W. Witczak-Krempa, Multiparty entanglement microscopy of quantum Ising models in one, two, and three dimensions, *Phys. Rev. B* **111**, 245108 (2025).
 - [41] M. Song, T.-T. Wang, L. Lyu, W. Witczak-Krempa, and Z. Y. Meng, Entanglement architecture of beyond-Landau quantum criticality, *arXiv e-prints*, [arXiv:2509.09983](https://arxiv.org/abs/2509.09983) (2025).
 - [42] A. Scheie, P. Laurell, A. M. Samarakoon, B. Lake, S. E. Nagler, G. E. Granroth, S. Okamoto, G. Alvarez, and D. A. Tennant, Witnessing entanglement in quantum magnets using neutron scattering, *Phys. Rev. B* **103**, 224434 (2021).
 - [43] C. Zhou, Z. Zhou, F. Desrochers, Y. B. Kim, and Z. Y. Meng, Quantum Fisher Information as a Thermal and Dynamical Probe in Frustrated Magnets: Insights from Quantum Spin Ice, *arXiv e-prints*, [arXiv:2510.14813](https://arxiv.org/abs/2510.14813) (2025).
 - [44] T. Shimokawa, S. Sabharwal, and N. Shannon, Can experimentally-accessible measures of entanglement distinguish quantum spin liquids from disorder-driven “random singlet” phases ?, *arXiv e-prints*, [arXiv:2505.11874](https://arxiv.org/abs/2505.11874) (2025).
 - [45] T.-T. Wang, M. Song, Z. Y. Meng, and T. Grover, Analog of Topological Entanglement Entropy for Mixed States, *PRX Quantum* **6**, 010358 (2025).
 - [46] Beijing PARATERA Tech CO.,Ltd .
 - [47] <http://www.nhr-verein.de/en/our-partners> .
 - [48] L. D. Landau *et al.*, On the theory of phase transitions, *Zh. eksp. teor. Fiz* **7**, 926 (1937).
 - [49] K. G. Wilson and M. E. Fisher, Critical Exponents in 3.99 Dimensions, *Phys. Rev. Lett.* **28**, 240 (1972).
 - [50] C. Jarzynski, Nonequilibrium Equality for Free Energy Differences, *Phys. Rev. Lett.* **78**, 2690 (1997).

Supplemental Material for “Precise computation of universal corner entanglement entropy at 2+1 dimension: From Ising to Gaussian quantum critical points”

In Sec. I, we provide the details in the RG flow analysis from the Gaussian fixed point to the Ising CFT.

In Sec. II, we provide the details of non-equilibrium method in finite temperature stochastic series expansion QMC framework, which are another method that can steadily extract the subtracted corner entanglement entropy (SCEE). We would introduce the details of the method, empirical scaling study of quench and benchmarking the results in main text against the result obtained via non-equilibrium method at $K = 160$ and 320 .

In Sec. III, we compare the results of physical observables in the conventional σ_z basis and bubble basis in the transverse field Ising model to prove the correctness of the bubble basis.

I. RG FLOW FROM THE GAUSSIAN FIXED POINT TO THE ISING CFT

In this section, we review the standard picture for the RG flow from the Gaussian fixed point to the Ising CFT. We first discuss Landau’s mean field theory analysis [48]. Since we are dealing with spontaneous Z_2 symmetry breaking, we can approximate the free energy as

$$F(\phi) = \frac{m^2}{2}\phi^2 + \frac{\lambda_4}{4!}\phi^4 + \frac{\lambda_6}{6!}\phi^6 + \dots \quad (S1)$$

Here ϕ is the order parameter for the symmetry breaking. Assume $\lambda_6 > 0$. When $m^2 > 0$, the free energy has a single minimum, corresponding to the disordered phase (PM phase). When $m^2 < 0$, the free energy have two minima, corresponding to the Z_2 symmetry breaking phase (FM phase). The order of the phase transition depends on the sign of λ_4 . When $\lambda_4 > 0$, the phase transition is second order. When $\lambda_4 < 0$, the phase transition is first order. This phase diagram from Landau’s theory agrees with the phase diagram in Fig. I (a) from our numerical simulation. Changing m^2 and λ_4 corresponds to moving perpendicularly or parallel to the phase separation line respectively.

Landau’s mean field theory analysis does not take into account the thermal/quantum fluctuations. To take them into account we should instead use the language of quantum field theory. This was first understood in the seminal paper by Wilson and Fisher [49], where they studied the renormalization group flow of the field theory:

$$S = \int d^D x \frac{1}{2}(\nabla_i \phi)^2 + \frac{1}{2}m^2\phi^2 + \frac{1}{4!}\lambda_4\phi^4. \quad (S2)$$

in $D = 4 - \epsilon$ dimensions. Setting $m^2 = 0$, the beta function of the coupling constant λ_4 is

$$l \frac{d\lambda_4}{dl} = \epsilon\lambda_4 - \frac{3}{16\pi^2}\lambda_4^2 + \dots \quad (S3)$$

Here l is the characteristic length scale. The beta function tells us how the coupling constant evolves as we change the length scale. The thermal dynamic limit of lattice models corresponds to large scale physics, that is $l \rightarrow \infty$. Higher order coupling terms, such as ϕ^6 terms can be neglected because they are irrelevant, and becomes less important in the $l \rightarrow \infty$. The beta function have two fixed points

$$\lambda_4 = 0, \quad \text{and} \quad \lambda_4 = \frac{16\pi^2}{3}\epsilon. \quad (S4)$$

The fixed point at $\lambda_4 = 0$ is a Gaussian fixed point, which corresponds to the tricritical point in Fig. I (a). The second fixed point is genuinely interacting, which corresponds to 2nd order Ising phase transition line in Fig. I (a). To study the physics in the physical dimension, we need to set $\epsilon = 1$. At the Gaussian point, the logarithmic correction to the entanglement entropy arising from sharp corners is well-established [4, 5], due to the fact that Gaussian theories are easier to deal with. At the interacting point, on the other hand, we are not aware of any reliable theoretical calculation to get the logarithmic correction. We benchmark our algorithm at the Gaussian fixed point, and then measure this quantity at the Ising fixed point.

II. NON-EQUILIBRIUM METHOD

A. Details of extracting SCEE with non-equilibrium method

Here, we demonstrate the details of the non-equilibrium method. The discussion of this section follows closely with those in Refs [3, 13, 15, 18, 22].

We introduce a partition function definition $Z_{A_1-A_2}(\lambda)$ parameterized by λ , where $Z(\lambda)$ is defined as the summation of collections for partition function Z_B weighted by binomial factor $g_A(\lambda, N_B) = \lambda^{N_B}(1-\lambda)^{N_{A_1}-N_{A_2}-N_B}$, where in the context of lattice model, N_{A_1} is the number of sites in entanglement region A_1 and N_B is the number of sites in the growing region. Typically, $N_B \leq N_{A_1} - N_{A_2}$. The definitions of A_1 and A_2 are illustrated in Fig. 1(a).

The partition function can therefore be written as,

$$Z_{A_1-A_2}(\lambda) = \sum_{B \subseteq (A_1-A_2)} \lambda^{N_B} (1-\lambda)^{N_{A_1}-N_{A_2}-N_B} Z_{B+A_2} = \sum_{B \subseteq (A_1-A_2)} g_A(\lambda, N_B) Z_{B+A_2}. \quad (\text{S5})$$

With the definition Eq. (S5), the SCEE can therefore be written as $S_s = -\ln\left(\frac{Z(\lambda=1)}{Z(\lambda=0)}\right)$ and it can be further rewritten it to an integral expression $S_s = -\int_0^1 d\lambda \frac{\partial \ln Z(\lambda)}{\partial \lambda}$. On the other hand, as the free energy F of a canonical ensemble can be written as $F = -\frac{1}{\beta} \ln(Z)$, where $\beta \equiv \frac{1}{k_B T}$. The ratio of $Z(\lambda=1)$ and $Z(\lambda=0)$ can be expressed as,

$$e^{-\beta \Delta F} = \frac{Z(\lambda=1)}{Z(\lambda=0)}. \quad (\text{S6})$$

By Jarzynski's equality [50], $\langle e^{-\beta W_A} \rangle = e^{\beta \Delta F}$, we can rewrite the expression (S6) as follows,

$$\begin{aligned} \langle e^{-\beta W_A} \rangle &= \frac{Z(\lambda=1)}{Z(\lambda=0)}, \\ -\ln(\langle e^{-\beta W_A} \rangle) &= -\ln\left(\frac{Z(\lambda=1)}{Z(\lambda=0)}\right), \\ S_s &= -\ln(\langle e^{-\beta W_A} \rangle), \end{aligned} \quad (\text{S7})$$

and the total work done W_A in the tunneling process from $Z(\lambda=0)$ to $Z(\lambda=1)$ is,

$$-\beta W_A = \int_0^1 dt \frac{d\lambda}{dt} \frac{\partial \ln g_A(\lambda(t), N_B(t))}{\partial \lambda} \quad (\text{S8})$$

where $\frac{d\lambda}{dt}$ is set to 1 throughout this section.

B. Empirical scaling study of quench time in non-equilibrium method

As mentioned in Sec II A, under the non-equilibrium method framework, the SCEE is related to the total work performed. This relationship is illustrated in Eq. (S8) along the tunneling process from $Z(\lambda=0)$ to $Z(\lambda=1)$. The number of steps used to discretize the integral in Eq. (S8) is hereafter referred to as the *quench steps*. The total number of quench steps $Q_t \sim 10^7$, for all L in Refs. [3, 22]. Nevertheless, the quench steps are relatively large for smaller L . We have conducted an empirical scaling study of quench steps and L to establish a benchmark for controlling the coefficient of variation (CV) to a sufficiently small value with an appropriate number of quench steps for a given L , i.e. $Q_t(L, CV)$.

The approximated expression of the coefficient of variation (CV) derivation follows closely the discussion in Ref. [1]. The workdone $-\beta W$ in the non-equilibrium framework and the SCEE S_s are related as $e^{-S_s} = \langle e^{-\beta W_A} \rangle$ and the coefficient of variation (CV) of e^{-S_s} is defined as the ratio of population standard deviation $\sigma_{e^{-S_s}}$ to the population mean $\mu_{e^{-S_s}}$ of e^{-S_s} , where $CV[e^{-S_s}] = \frac{\sigma_{e^{-S_s}}}{\mu_{e^{-S_s}}}$. We then denote $\sigma_{-\beta W_A}$ and $\mu_{-\beta W_A}$ as the population standard deviation and population mean of $-\beta W_A$ respectively. If $-\beta W_A$ follows normal distribution, which is shown in Fig. S1, we can express the $CV[e^{-S_s}]$ in terms of $\sigma_{-\beta W_A}$ and $\mu_{-\beta W_A}$ as follows,

$$\begin{aligned} CV[e^{-S_s}] &= \frac{\sqrt{(e^{\sigma_{-\beta W_A}^2} - 1)e^{(2\mu_{-\beta W_A} + \sigma_{-\beta W_A}^2)}}}{e^{\mu_{-\beta W_A} + \sigma_{-\beta W_A}^2/2}} \\ &= \sqrt{e^{\sigma_{-\beta W_A}^2} - 1} \\ &= \sqrt{(1 + \sigma_{-\beta W}^2 + \dots) - 1} \\ &\approx \sigma_{-\beta W}. \end{aligned} \quad (\text{S9})$$

The final step of Eq. (S9) is obtained by truncating the higher-order terms. Given the number of quench steps we employed, this approach is justified because $\sigma_{-\beta W_A}$ is significantly less than 1. After that, we denote $s_{-\beta W_A}$ as the sample standard deviation of $-\beta W_A$. Since $s_{-\beta W_A}$ is an unbiased estimator of $\sigma_{-\beta W_A}$ and from Eq. (S9), we know that $s_{-\beta W_A} \approx CV[e^{-S_s}]$ and we will replace $CV[e^{-S_s}]$ by $s_{-\beta W_A}$ in the following analysis.

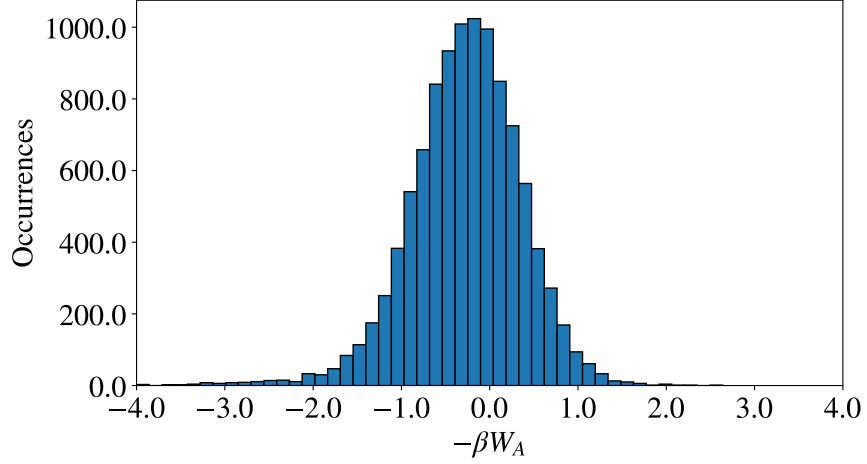


FIG. S1. **Distribution of the work done.** Example plot of $-\beta W_A$ distribution with $Q_t = 5000$ of $L = 12$ system at $K = 320$, $h = 1260$ (along the phase boundary in Fig. I (a)). The distribution of $-\beta W_A$ follows roughly a normal distribution.

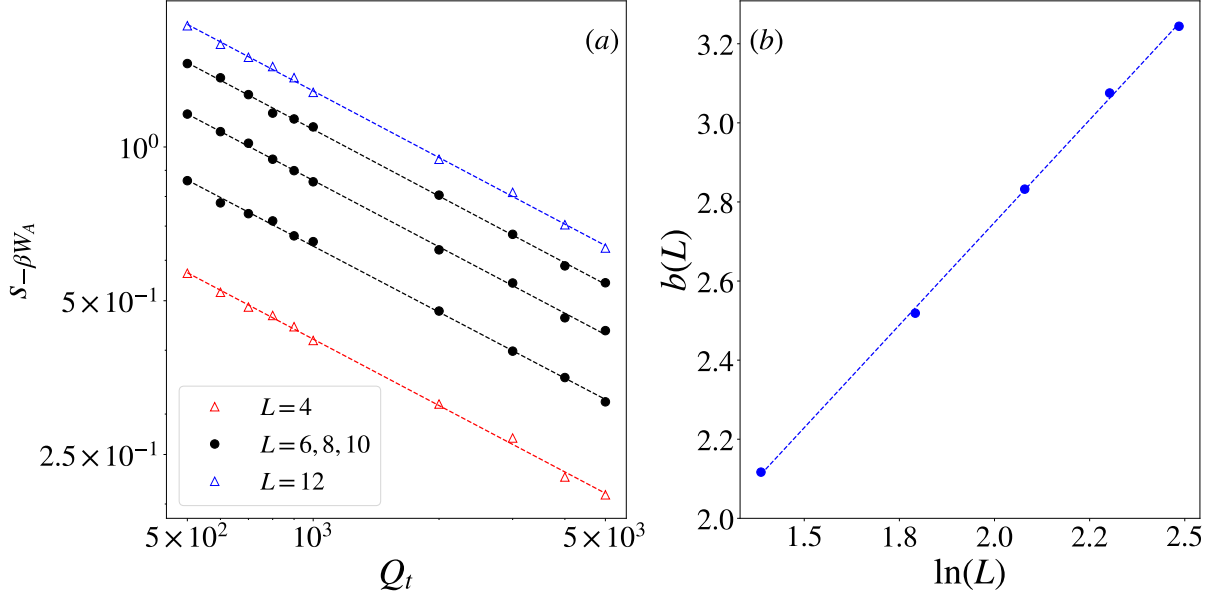


FIG. S2. **Result of the empirical scaling analysis study** (a) The sample standard deviation $s_{-\beta W_A}$ against the total number of quench steps Q_t . The average slope in (a) of the linear fitting $\bar{a} = -0.431(5)$. (b) The intercept $b(L)$ in (a) as a function of L . The slope obtained from linear fitting is $b_m = 1.03(1)$, and the intercept is $b_0 = 0.67(2)$.

By observing the log-log plot in Fig. S2, we can conclude the empirical relation between the total number of quench steps and $s_{-\beta W_A}$ (or CV) as $\ln(s_{-\beta W_A}) = \bar{a} \ln Q_t + b_m \ln L + b_0$. Rearranging the terms and putting the relation $s_{-\beta W_A} \approx CV[e^{-S_s}]$ back, we will get the $Q_t(L, CV) = (CV[e^{-S_s}]e^{-b_0}L^{-b_m})^{1/\bar{a}}$. We set $CV[e^{-S_s}] = \frac{0.05}{\sqrt{L}}$ for all L and estimate the total number of quench steps Q_t needed for $K = 320$ data in (b) of Fig. S3. We also notice that the quench step requirement are more stringent for larger K . Therefore, using the quench steps estimated at $K = 320$ in smaller K simulation would be sufficient.

C. Benchmarking the non-equilibrium methods against projector quantum Monte Carlo result

To examine the correctness the of PQMC result at large K regime in the main text, we employ the non-equilibrium method to extract the subtracted entanglement entropy S_s . We perform the simulation at phase transition h_c of $K = 160$ and $K = 320$, which are $h_c = 633$ and $h_c = 1260$, respectively. The results are shown in Fig. S3. From the figure, we can see that the results in main text and the result obtained via the non-equilibrium method are fairly close.

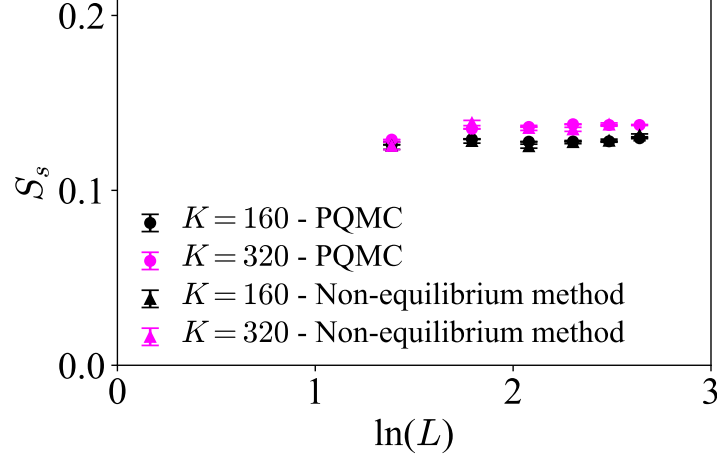


FIG. S3. **Comparing the result in main text and the result of the non-equilibrium method.** The subtracted entanglement entropy S_s are extracted at $(K_c, h_c) = (160, 633)$ and $(K_c, h_c) = (320, 1260)$ with both non-equilibrium and PQMC method. $L_{min} = 4$ and $L_{max} = 14$ for both simulations performed at $K = 160$ and 320 .

III. BENCHMARK OF σ_z AND BUBBLE BASES OF TRANSVERSE FIELD ISING MODEL WITH PQMC

In this section, we provide the benchmark results of the phase transition with both σ_z basis and the bubble basis, in the PQMC.

A. Definition

The expectation value of magnetization in PQMC is defined as follows:

$$\langle M \rangle = \frac{\langle \alpha_l^m | \sum_{n=0}^N \hat{\sigma}_n^z | \alpha_r^m \rangle}{\langle \alpha_l^m | \alpha_r^m \rangle}. \quad (\text{S10})$$

For the spin σ_z basis, it is trivial to evaluate this expectation value. However, in the bubble basis, if one evaluates this value directly, results of $M = 0$ would be obtained for every possible states which doesn't give any useful information. Therefore, to tackle this problem, an extra step is added to obtain this value. A bubble, was first in a superposition of sites of up spins and down spins. By collapsing the bubble into up spins or down spins with $P(\uparrow) = 1/2$ and $P(\downarrow) = 1/2$, $\langle M \rangle = [-1, 1]$ instead of 0. In this way, the expectation of magnetization can be sampled correctly. For a more practical sample, please refer to Fig. S4.

B. Comparison between the Bubble and Spin Basis

To examine the correctness of the TFIM in the Bubble Basis, the Binder cumulant was evaluated in the Bubble Basis and was used to find the phase transition point of the TFIM. The h_c and ν of $(2+1)$ D TFIM is known to be 3.044 and 0.629 respectively. The results are given in Fig. S5, where Fig. S5 (a) shows the Binder cumulant vs h graph near the phase transition point, the crossing point of the Binder cumulant is at $h \approx 3.01$ compare with the $h_c = 3.044$ of $(2+1)$ D TFIM denotes by a vertical grey dotted line. It is fairly close to the expected result, and Fig. S5 (b) shows the heat map of the R statistic for the data collapse, evaluated over a range of ν and h . From the heat map, it can be seen that the $h_c \approx 3.01$ and $\nu \approx 0.62$, these results match nicely

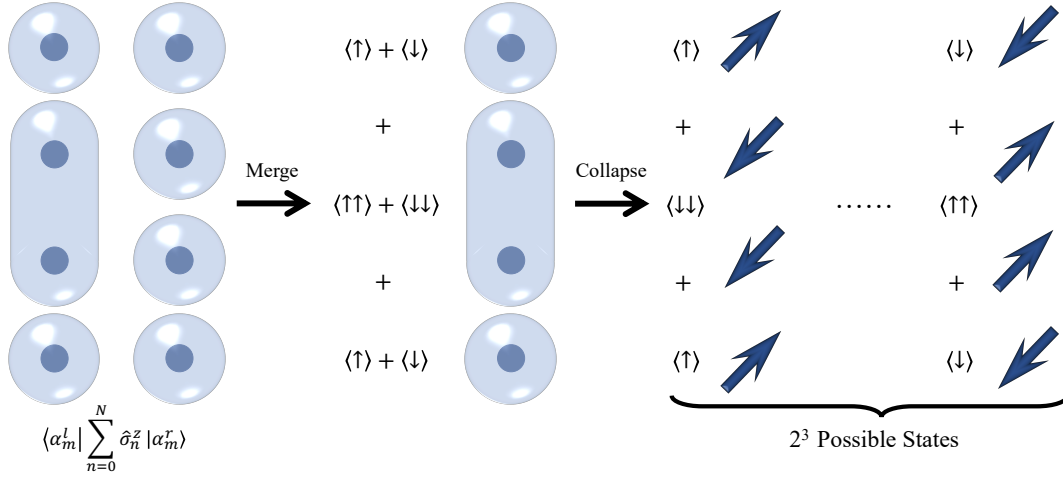


FIG. S4. A figure demonstrates how the states in Bubble basis are collapsing into Spin basis. At the left-most panel, the bubbles represent the states in terms of Bubble Basis. Then a step of merging the $\langle \alpha_m^L |$ and $|\alpha_m^r \rangle$ was performed. However, if $\langle M \rangle$ was calculated directly in this step, it can be easily seen that it equals 0 no matter what the state is. Therefore, an extra step of collapsing was added. By randomly selecting the state of a bubble to all up spins or to all down spins with $P(\uparrow) = 1/2$ and $P(\downarrow) = 1/2$ and by adding all the spins together, a sample of $\langle M \rangle$ can then be obtained as in Spin basis.

with the expected results for the (2+1)d Ising QCP. [34, 35]. It is one of the evidence that the Bubble Basis is able to give correct results.

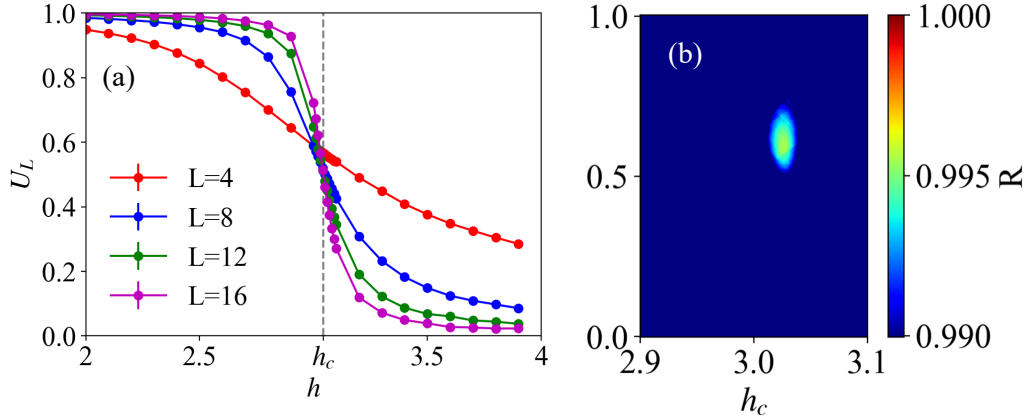


FIG. S5. Finite-size scaling analysis of the (2+1)d Ising QCP sampled with bubble basis. (a) Binder cumulant U_L as a function of h for different system sizes up to $L = 16$. The crossing point of the curves determines the critical field (b) Heat map of the R statistic for the data collapse, evaluated over a range of ν and h_c values. The optimal region of high R aligns with $\nu = 0.63$.